JACS
JOURNAL OF THE AMERICAN CHEMICAL SOCIETY

Article

pubs.acs.org/JACS

Highly Oriented Low-Dimensional Tin Halide Perovskites with Enhanced Stability and Photovoltaic Performance

Yuqin Liao,[†,‡,⊥] Hefei Liu,[‡,⊥] Wenjia Zhou,[‡] Dongwen Yang,[§] Yuequn Shang,[‡] Zhifang Shi,[‡] Binghan Li,[‡] Xianyuan Jiang,[‡] Lijun Zhang,*[,§] Li Na Quan,[∥] Rafael Quintero-Bermudez,[∥] Brandon R. Sutherland,[∥] Qixi Mi,[‡] Edward H. Sargent,[∥] and Zhijun Ning*[,‡]

[‡]School of Physical Science and Technology, ShanghaiTech University, 100 Haike Road, Shanghai 201210, China

[§]Key Laboratory of Automobile Materials of MOE, State Key Laboratory of Superhard Materials, and College of Materials Science, Jilin University, Changchun 130012, China

[†]Shanghai Institute of Microsystem and Information Technology, Chinese Academy of Sciences, 865 Changning Road, Shanghai 200050, China

[∥]Department of Electrical and Computer Engineering, University of Toronto, 10 King's College Road, Toronto, Ontario M5S 3G4, Canada

S *Supporting Information*

ABSTRACT: The low toxicity and a near-ideal choice of bandgap make tin perovskite an attractive alternative to lead perovskite in low cost solar cells. However, the development of Sn perovskite solar cells has been impeded by their extremely poor stability when exposed to oxygen. We report low-dimensional Sn perovskites that exhibit markedly enhanced air stability in comparison with their 3D counterparts. The reduced degradation under air exposure is attributed to the improved thermodynamic stability after dimensional reduction, the encapsulating organic ligands, and the compact perovskite film preventing oxygen ingress. We then explore these highly oriented low-dimensional Sn perovskite films in solar cells. The perpendicular growth of the perovskite domains between electrodes allows efficient charge carrier transport, leading to power conversion efficiencies of 5.94% without the requirement of further device structure engineering. We tracked the performance of unencapsulated devices over 100 h and found no appreciable decay in efficiency. These findings raise the prospects of pure Sn perovskites for solar cells application.

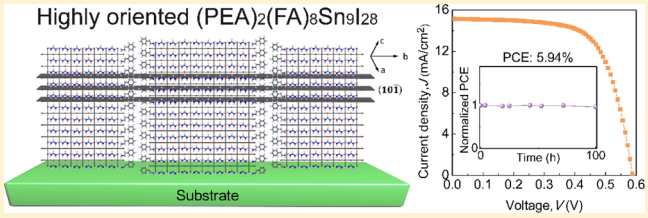

INTRODUCTION

Organic−inorganic hybrid halide perovskite materials have been extensively investigated owing to their impressive optical and electronic attributes such as an extremely low density of defects, excellent carrier transport, and strong light harvesting capability and luminescence intensity, as well as facile solution fabrication processing.[1−8] As perovskite film fabrication and device structure design have progressed, the power conversion efficiency (PCE) of solar cells based on lead perovskites has rapidly ascended from 3.8% to 22.1% in recent years.[9−13] However, Pb-based perovskites are environmentally toxic, and are subject to international waste disposal regulations. The impressive progress of Pb perovskite photovoltaics prompted the search for novel Pb-free halide perovskite materials. Perovskites based on tin, bismuth, and copper metals have been intensively explored recently.[14−17] These materials show promise for reduced environmental toxicity, especially for wearable and disposable devices. In addition, the bandgap tunability of some of these promising Pb-free halide perovskites enables extending the light harvesting range to the infrared (IR) region, an important feature for many solar cells, optical communications, and light-sensing applications. Hybrid Sn perovskites such as methylammonium tin iodide ($MASnI_3$) and formamidinium tin iodide ($FASnI_3$), have absorption onsets at longer IR wavelengths compared to their Pb-based counterparts, and have been studied for solar cells.[14,18−22] Combining Sn and Pb, graded-structure solar cells were fabricated that show a large photocurrent of 40 mA/cm^2 and PCE close to 21.7%.[23] To date, solar cells based on pure Sn perovskites have yet to realize the high-efficiency achieved in Pb-based devices. $MASnI_3$ perovskite solar cells (PSCs) showed PCE of approximately 6%,[18,19] and $FASnI_3$ PSCs demonstrated efficiencies up to 6.2%.[14,21,22]

Most Sn PSCs suffer from extremely poor stability and reproducibility due to the instantaneous oxidation of Sn^{2+} to Sn^{4+} (even in nitrogen atmosphere) and uncontrollable crystal growth. The use of tin fluoride (SnF_2) additives[20] and the introduction of a tin iodide−dimethyl sulfoxide (SnI_2−DMSO) complex during the crystallization process relieved the oxidation and decreased the crystallization rate.[24] However, the films degraded in minutes when exposed to ambient

Received: February 23, 2017
Published: April 24, 2017

DOI: 10.1021/jacs.7b01815
J. Am. Chem. Soc. XXXX, XXX, XXX−XXX

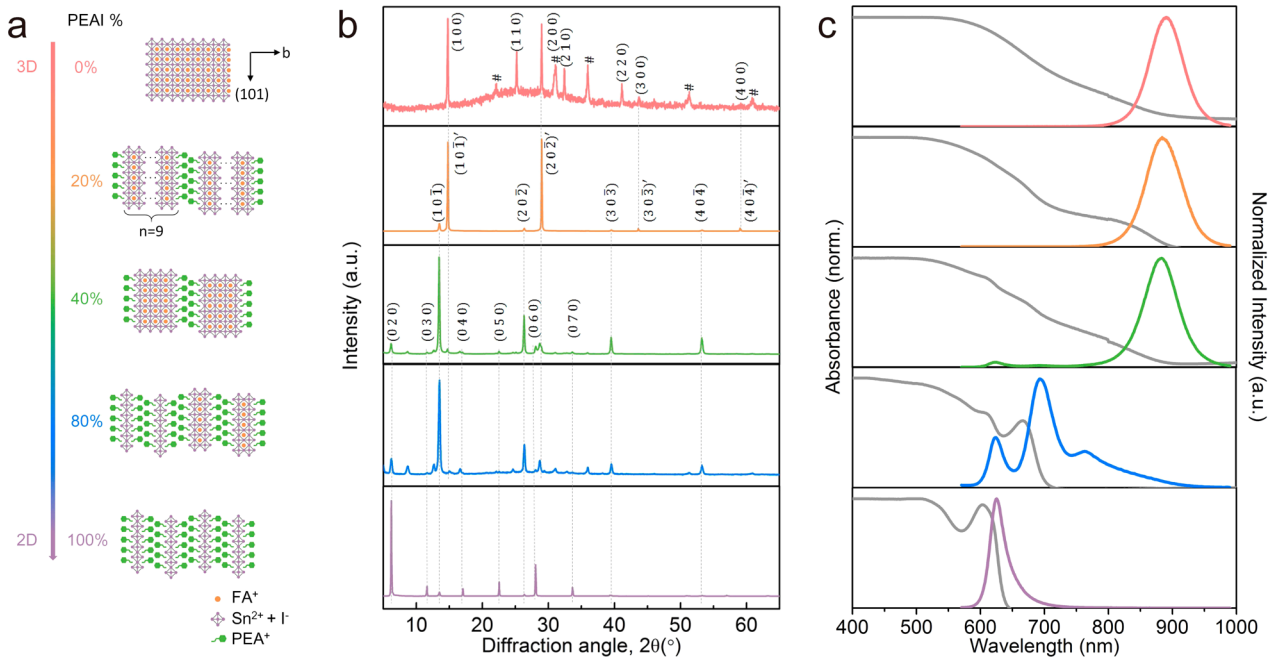

Figure 1. (a) Schematic structures of $FASnI_3$ and $(PEA)_2SnI_4$, and mixed FA-PEA tin perovskites. The PEA% labels indicate the mole percentage of PEA as a fraction the total organic cation composition; the labels also apply to panels b and c. Letter *n* denotes the average layers of tin iodide octahedra in nanolayers. (b) XRD spectra for Sn perovskite films with different PEA ratios. The peaks of $FASnI_3$ were indexed in a quasi-cubic system, while peaks of other films are indexed in an orthorhombic system. Miller indices followed by a "prime" symbol, like $(10\bar{1})'$, represent lattice planes in crystal domains in which the in-plane lattice parameters approach bulk perovskite ($n > 5$), whereas lattice planes in other grains are indexed without an extra symbol, like $(10\bar{1})$. A # indicates the diffraction peaks of ITO. (c) Normalized absorbance (gray curves, left axis) and photoluminescence (colorful curves, right axis) spectra of the investigated thin films.

atmosphere, and encapsulation is necessary for stability tracking in nitrogen environment. The development of more effective strategies is therefore imperative to improve the device stability.

The adsorption of water or oxygen molecules onto perovskites is generally regarded as the source of crystal decomposition.[25−29] The separation of perovskite from moisture and oxygen via encapsulation can significantly improve the device stability.[29] Recently, the inclusion of large ammonium cations, such as butylammonium (BA) and phenylethylammonium (PEA), have been shown to block moisture ingress at the boundaries of Pb-based perovskite nanolayers, giving rise to unprecedented high stability of films and devices.[30−37] Similar to Pb perovskites, two-dimensional (2D) Sn perovskites show much better stability than three-dimensional (3D) films.[30,31] However, there is no report to date demonstrating low-dimensional Sn perovskites in solar cells. This is likely ascribed to the poor carrier transport properties of these films as a result of their quantum well structure.[31,33,34] We hypothesized that orientated perovskite films that are vertically grown would form a continuous carrier transport pathway free of confinement barrier impediment, enabling improved photovoltaic performance.[37]

In this work, by using appropriate ratio of PEA as encapsulating molecules, we realize highly orientated growth of low-dimensional $FASnI_3$ perovskite films on nickel oxide (NiO_x) substrates, leading to greatly enhanced air stability. We subsequently fabricated planar inverted solar cells using [6,6]-phenyl-C_{61}-butyric acid methyl ester (PCBM) as an electron transporting layer, achieving solar cells efficiency up to 5.94%. The device retains its performance for over 100 h without encapsulation.

RESULTS AND DISCUSSION

We grew Sn perovskite films using a one-step spin coating method. Typically, a mixture of formamidinium iodide (FAI), SnI_2, SnF_2, and a varying amount of phenylethylammonium iodide (PEAI) dissolved in an *N*,*N*-dimethylformamide (DMF) and DMSO mixed solvent was spin-cast onto a NiO_x substrate. This was followed by the addition of toluene as an antisolvent (for details, see Experimental Details). With the addition of PEA, the $FASnI_3$ bulk perovskite is separated into 2D nanolayers (Figure 1a). Layers of metal-halide octahedra are sliced along the (100) direction in the original quasi-cubic $FASnI_3$, and the residual structures between every two cut layers are isolated by bilayers of PEA. The layered perovskites have an orthorhombic structure with *b*-axis perpendicular to the planes of the PEA bilayer.[30] The structure is given as $(PEA)_2(FA)_{n-1}Sn_nI_{3n+1}$, where *n* represents the number of tin iodide layers in the structural unit, which is tuned by changing the stoichiometric ratio of PEA to FA from 0% to 100%. Mixed FA-PEA samples exhibit two peaks near 14° in X-ray diffraction (XRD) spectra (Figure 1b). The $(10\bar{1})'$ peak sharing the same angle with the (100) peak in quasi-cubic $FASnI_3$ is contributed by the multilayer 2D component ($n > 5$), whose structure evolves to its 3D analogue as *n* increases.[30] The emerging $(10\bar{1})$ peak at a lower angle originates from the distortion of in-plane lattice parameters (*a* and *c*) as *n* decreases. As increasing amounts of PEA are incorporated into the film, the relative change in intensity of the two peaks reflects the increasing ratio of few-nanolayers ($n = 1−5$) to multilayer ($n > 5$) ones. Films with over 40% PEA exhibit peaks corresponding to the (020) facet of $(PEA)_2SnI_4$, which indicates the presence of single-layer 2D compounds. Small-angle XRD patterns for $FASnI_3$ and 20% PEA sample are shown in Figure S1. The diffraction peak at 4°

DOI: 10.1021/jacs.7b01815
J. Am. Chem. Soc. XXXX, XXX, XXX−XXX

for 20% PEA film features the (010) facet of 2D perovskite. This peak is not observed for the film without the addition of PEA. Such result provides direct evidence for the formation of low-dimensional structure. In sum, the PEA-FA mixed Sn perovskite films are mixtures of 2D compounds with different layers, and the composition of these films completes the transition through pure 3D, 2D−3D mixture, to pure 2D as the PEA ratio increases from 0 to 100%.

The change in composition with increasing PEA ratio was confirmed by analysis of the photoluminescence (PL) and absorbance spectra (UV−vis), as shown in Figure 1c. The continuous blue shift (890 to 625 nm) of the PL peak with increasing PEA ratio demonstrates the formation of a low-dimensional perovskite phase and a decreasing thickness of the perovskite nanolayers.[38] The PL spectra was pumped from both top (perovskite/air interface) and bottom surfaces (perovskite/substrate interface) (Figure S2 and Figure S3) and collected from the opposite side. When pumped from the bottom interface, PL peaks are observed at 625, 693, and 762 nm for samples with over 40% PEA. These are signatures of 2D perovskites of one, two, and three layers, respectively, similar to what has been observed in 2D Pb perovskites.[33] The multiple PL peaks observed from films with 40% and 80% PEA provide evidence that these films are a mixture of phases. Compared to the spectra obtained from bottom interface excitation, the top interface measurements do not show emission peaks at 625 or 693 nm in the 40% PEA film. This suggests that small n value 2D nanolayers prefer to locate at the bottom of these films.[36] Emergence of such nonhomogeneous compositional gradients under the higher PEA concentration may be attributed to the difference in solubility of PEAI and FAI precursors in the antisolvent we used. Similar behavior has also been reported in Pb-based 2D perovskites.[36] The absorption spectra further confirm the formation of low-dimensional perovskite phases. A pure $FASnI_3$ sample shows an absorption edge near 950 nm, while single-layer 2D $(PEA)_2SnI_4$ samples display a sharp excitonic absorption peak at 603 nm; and 40% and 80% PEA samples exhibit an additional peak at 670 nm. The position and intensity of these absorption peaks are consistent with the PL peaks, confirming the formation of a 2D perovskite phase.

From XRD (Figure 1b), the (110), (210), and (220) peaks in $FASnI_3$ are absent from the 20% PEA sample, implying the preferential orientation of the crystal grains. We noted that 2D perovskites layers can be oriented along the direction either parallel or perpendicular to the surface of substrate.[34,36,37] To further confirm the orientation of the 2D Sn perovskite, we performed a grazing-incidence wide-angle X-ray scattering (GIWAXS) analysis using synchrotron radiation. The scattering patterns of 0% and 20% PEA films are shown in Figure 2a,b. The 0% PEA sample (Figure 2a) displays Debye−Scherrer rings with an isotropical intensity distribution, indicating complete randomness in the orientation of the crystal grains. By contrast, in the 20% sample (Figure 2b), sharp and discrete Bragg spots are observed. This indicates that crystal grains are highly oriented, with their $(10\bar{1})$ planes parallel to the substrate surface (Figure 2c). Films with higher PEA ratios exhibit diffraction rings with stronger intensity in the q_z direction (Figure S4). This indicates considerable randomness in the orientation of the crystal domains. The spots closer to the central point in the q_z direction, compared to those in the image of 20% film, feature the preferential orientation of PEA bilayers parallel to the substrate. We assume that the

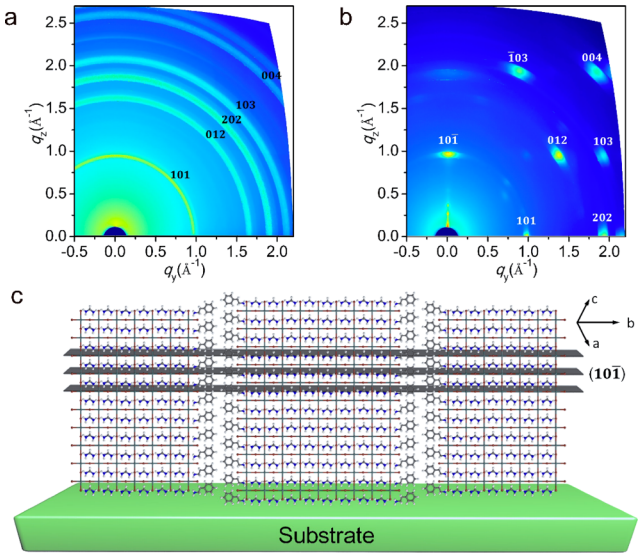

Figure 2. GIWAXS images for $FASnI_3$ film (a) and 20% PEA film (b) with Miller indices (orthorhombic system) of prominent peaks. (c) Schematic illustration of the (101) plane of a $(PEA)_2(FA)_8Sn_9I_{28}$ (n = 9) 2D perovskite crystal.

orientation growth perpendicular to the substrate is thermodynamically favorable only in the 20% PEA condition.

The perpendicular orientation growth of perovskite facilitates the growth of compact and smooth films, as indicated by the scanning electron microscopy (SEM) image (Figure 3). In

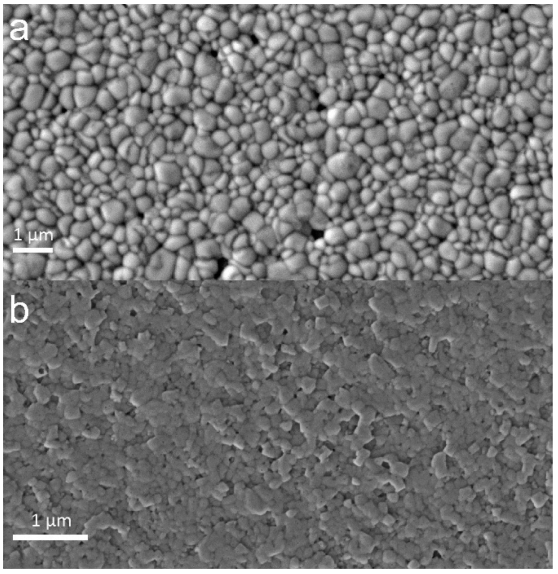

Figure 3. SEM images of $FASnI_3$ (a) and 20% PEA (b) films. The latter one displays lower pinhole density, more compact and smoother surface morphology, and more homogeneous grain size.

contrast, 3D $FASnI_3$ films are quite rough due to uncontrolled crystal growth. Smooth and dense films are beneficial for protecting the film from oxygen infiltration, which mitigates perovskite oxidation. In addition, in the 20% PEA film with PEA bilayers perpendicular to substrate, the pure inorganic framework similar to 3D $FASnI_3$[31] is sufficiently extended between the two electrodes. This suggests promise for carrier transport that is comparable to bulk perovskites. All these

DOI: 10.1021/jacs.7b01815
J. Am. Chem. Soc. XXXX, XXX, XXX−XXX

characters make the 20% PEA films promising for fabrication of planar solar cells with high efficiency and stability.

We compared the Sn^{4+} content in the $FASnI_3$ and 20% PEA films using X-ray photoelectron spectroscopy (XPS). To exclude the effect of surface oxidation, samples were etched before the measurement (Figure S6 and Table S1). Figure 4a shows the XPS spectra of the Sn 3d bands of $FASnI_3$ and 20% PEA films with a 30 s etching time. The two peaks deconvoluted from the measured spectra at 486.7 and 487.4 eV are associated with Sn^{2+} and Sn^{4+}, respectively.[39−41] The Sn^{4+} amount in the 20% PEA film is much lower than that in $FASnI_3$, implying the low-dimensional structure prevents Sn^{2+} from oxidation during film fabrication.

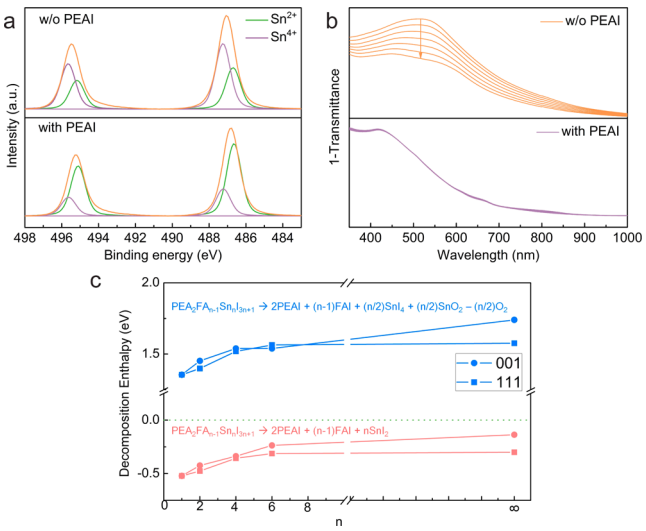

Figure 4. (a) XPS Sn 3d spectra of films without PEA and with 20% PEA (orange). The two peaks deconvoluted from the measured spectra at 486.7 and 487.4 eV are associated with Sn^{2+} (green) and Sn^{4+} (purple), respectively. The etching time is 30 s. (b) Evolution of the transmittance spectra of films without PEA and with 20% PEA exposed to ambient atmosphere in 30 min. (c) Stability of $(PEA)_2(FA)_{n-1}Sn_nI_{3n+1}$ indicated by the calculated decomposition enthalpy ΔH_{dec} (in eV per Sn atom). The results corresponding to the decomposition pathways involving merely the Sn^{2+} compounds and the Sn^{4+} compounds are shown with red and blue lines, respectively. Different orientations of FA molecules along (001) (circles) and (111) (squares) directions of the 3D quasi-cubic lattice are considered, giving qualitatively consistent results. The decreasing trend of ΔH_{dec} for both decomposition pathways as n decreases indicates the enhanced stability of 2D Sn based perovskites with increasing PEA content, which agrees with experimental observation.

To investigate the oxidation resistance of the films, an in situ UV−vis experiment in ambient environment was conducted to monitor the evolution of absorption spectra of thin films with time, as shown in Figure 4b. A significant decrease of absorbance over the whole spectrum region within a few minutes was observed for the $FASnI_3$ film, and the curve constantly shifts downward over a duration of 30 min. This indicates fast degradation of the sample, consistent with a previous report that 3D hybrid Sn perovskite films turned transparent within minutes of air exposure.[20] By contrast, the absorption spectra of the 20% PEA film did not change over a span of 30 min, indicating improved stability over the pure FA samples. Compared with the case of bulk 3D Sn perovskites, clearly the air stability of low-dimensional Sn perovskite films is substantially improved.

To probe the origin of the enhanced air stability of low-dimensional Sn perovskites $(PEA)_2(FA)_{n-1}Sn_nI_{3n+1}$, we performed first-principles density functional theory (DFT) calculations of materials thermodynamic stability with respect to possible disproportionation channels. The stability of one material can be indicated by the decomposition enthalpy (ΔH_{dec}) that is defined as the free energy difference between the target material to be evaluated and the possible decomposed products. Negative value of ΔH_{dec} corresponds to thermodynamically stable condition. Two decomposition pathways are considered: one involves only Sn^{2+} compounds,

$$PEA_2FA_{n-1}Sn_nI_{3n+1} \rightarrow 2PEAI + (n-1)FAI + nSnI_2 \quad (1)$$

the other involves only Sn^{4+} compounds to take into account the oxidation process,

$$PEA_2FA_{n-1}Sn_nI_{3n+1} \rightarrow 2PEAI + (n-1)FAI + \frac{n}{2}SnI_4 + \frac{n}{2}SnO_2 - \frac{n}{2}O_2 \quad (2)$$

The calculated ΔH_{dec} as a function of n for $(PEA)_2(FA)_{n-1}Sn_nI_{3n+1}$ is shown in Figure 4c and Table S2. Since the small FA molecules are randomly orientated at room-temperature because of the low rotation barrier, we considered the $(PEA)_2(FA)_{n-1}Sn_nI_{3n+1}$ structure with two different orientations of FA, i.e., along (001) and (111) directions of the 3D quasi-cubic lattice. Two cases give qualitatively consistent results. One observes that the $(PEA)_2(FA)_{n-1}Sn_nI_{3n+1}$ perovskites are stable with respect to the decomposition pathway (1) (with negative ΔH_{dec}), but unstable with respect to the decomposition pathway (2) (with positive ΔH_{dec}). This is in agreement with the experimentally observed tendency of the Sn based perovskites being prone to oxidation in air atmosphere.[23] As n decreases, the ΔH_{dec} with respect to the oxidation decomposition pathway (2) shows a substantial decrease. This suggests that the instability against the oxidation disproportionation process is suppressed. It is therefore the improved thermodynamic stability of 2D Sn perovskites that is responsible for their superior oxidation resistance. Additionally, the encapsulating organic PEA ligands and compact perovskite film also protect Sn^{2+} from contact with oxygen, further augmenting the oxidation resistance of 2D $(PEA)_2(FA)_{n-1}Sn_nI_{3n+1}$.

We further investigated the carrier transport properties of 20% PEA films. The carrier concentration of the 20% PEA film was measured by capacitance−voltage ($C-V$) studies (Figure S8, see details in Supporting Information). The $C-V$ curve demonstrates that 20% PEA films are p-type semiconductors, which is ascribed to a self-doping effect.[42] The carrier concentration is calculated to be 2.27×10^{17} cm^{-3}, remarkably lower than pure $FASnI_3$.[14] The underlying mechanism is the 2D PEA-containing perovskites with enhanced thermodynamic stability suppressing the formation of Sn^{4+} related defects that invokes self-doping process. This is supported by the low Sn^{4+} content in the 2D PEA-containing perovskite film as indicated by XPS measurement.

Space charge limited current (SCLC) studies were conducted to measure the carrier mobility of the perovskite films (see Supporting Information). The electron mobility was smaller than the hole mobility (Figure S9). To estimate the carrier lifetime, we performed fluorescence decay measurements using time-resolved fluorescence (TRF) spectroscopy by

DOI: 10.1021/jacs.7b01815
J. Am. Chem. Soc. XXXX, XXX, XXX−XXX

depositing 20% PEA perovskite layers onto ITO, NiO_x (hole quenching layer), and PCBM (electron quenching layer) (Figure S11). The carrier lifetime of the films on ITO is estimated to be 6.3 ns. In presence of the quenching layer (such as NiO_x), one of the carriers (hole for NiO_x) in active $(PEA)_2(FA)_{n-1}Sn_nI_{3n+1}$ layer can be quickly extracted by the quenching layer. This leads to decrease in the lifetime of this carrier, which is indicated by the reduced PL decay lifetime. Based on the PL decay measurement for the perovskite films on NiO_x and PCBM (Figure S11), the reduced carriers lifetime are 4.97 and 3.12 ns for hole and electron, respectively. The reduced carriers lifetime indicate efficient carrier transport in the $(PEA)_2(FA)_{n-1}Sn_nI_{3n+1}$ films.

We explored 20% PEA Sn perovskite films as light absorber for solar cells with an inverted planar architecture of ITO/NiO_x/Perovskite/PCBM/Al (Figure 5a). Here, NiO_x and PCBM serve as the hole and electron transport layers, respectively. The fabrication details can be found in Experimental Details. According to the cross-sectional SEM image of the device (Figure S12), the thicknesses of the perovskite, NiO_x, and PCBM layers are approximately 200, 50, and 100 nm, respectively. Meanwhile, we systematically studied the impact of SnF_2 concentration on films morphology and device performance. High density of pinholes were found in the films with too much or too little SnF_2. When 10% SnF_2 is included, compact and smooth films are formed, which yields the highest efficiency (Figure S13). We tested the device performance under simulated AM1.5G irradiation. The highest PCE reaches 5.94% (Figure 5a), with an open circuit voltage (V_{oc}) of 0.59 V, a short-circuit current density (J_{sc}) of 14.44 mA/cm^2, and fill factor (FF) of 69%. The V_{oc} is much higher than that of the best previously reported 3D $FASnI_3$ PSCs, which vary from 0.262 to 0.465 V.[14,21,22] The enhanced V_{oc} can be ascribed to the suppressed defect concentration induced by oxidation, as a result of the low-dimensional structure. The high FF value can be ascribed to suppressed defect-mediated carrier recombination, as well as balanced carrier transport.[43−46] The relatively low J_{sc} is likely related to the low carrier mobility, as well as charge recombination at the interface between the active layer and carrier transport layers. The external quantum efficiency (EQE) spectrum (Figure 5b) shows broad light harvesting, ranging out to 900 nm, and is consistent with the absorption spectrum. The integrated J_{sc} calculated from the EQE spectrum (14.57 mA/cm^2) agrees well with the value measured from the $J-V$ curve. Only slight hysteresis is observed for these devices, as shown in the $J-V$ curves with voltage scanned in both reverse and forward directions (Figure S14). These devices exhibit high reproducibility. From a sample set of 30 devices, the photovoltaic figures of merit ± one standard deviation are J_{sc}= 14.18 ± 1.29 mA/cm^2, V_{oc}= 0.583 ± 0.009 V, FF = 62.14 ± 4.77%, and PCE = 5.05 ± 0.56% (Figure 5c).

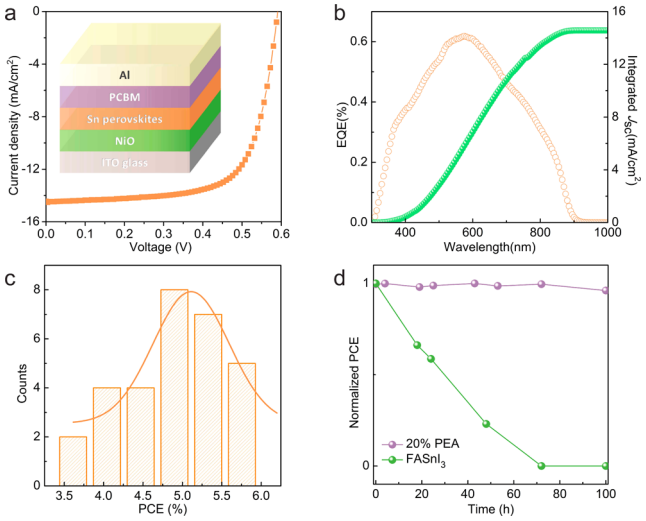

Figure 5. (a) Device architecture and current density−voltage ($J-V$) characteristics of the highest performance device. (b) EQE spectrum and EQE-based integrated J_{sc} of the highest performance device. (c) Statistics of the PCE distribution. Orange solid line denotes the Gaussian distribution fitting. (d) Normalized PCE of the unencapsulated device based on $FASnI_3$ and 20% PEA-doped perovskite film stored in a glovebox for over 100 h.

We tracked the device performance in the N_2 atmosphere glovebox without encapsulation. The PSCs based on the 3D $FASnI_3$ were fabricated for comparison (Figure S17 and Figure 5d). As clearly seen, while the efficiency of the 3D $FASnI_3$ PSC decays to 23% of its original value within 48 h, the efficiency of the 2D 20% PEA-containing perovskites PSC retains 96% of its initial value for over 100 h (Figure 5d). Possible explanation for the fast degradation of the 3D $FASnI_3$ PSC could be that a certain amount of oxygen and moisture exists in the glovebox filled with N_2, therefore the fast oxidation process still occurs to $FASnI_3$. This results ambiguously demonstrate that the dimensional reduction from the 3D $FASnI_3$ to the 2D $(PEA)_2(FA)_{n-1}Sn_nI_{3n+1}$ significantly improves materials stability and effectively suppresses oxidation disproportionation, resulting in stable device performance.

CONCLUSION

In summary, we fabricated low-dimensional tin halide perovskite thin films by utilizing PEA as an organic separating interlayer. The orientation of the perovskite domains can be modified through manipulating the PEA ratio, and a highly oriented perovskite film perpendicular to the substrate was realized with 20% PEA. The low-dimensional Sn perovskites exhibit significantly enhanced stability in air atmosphere compared to their three-dimensional counterparts. First-principles calculations indicate the higher intrinsic thermodynamic stability of low-dimensional Sn perovskites with respect to the oxidation disproportionation channel. The existence of large PEA molecules at the boundary of perovskite nanolayers, and the compact pinhole-free films achieved by manipulating the film composition, can block oxygen diffusion into the perovskite lattice. These factors jointly contribute to the improved oxidation resistance, resulting in improved materials air stability. In addition to the enhanced stability, the perpendicular growth of the highly oriented film enabled improved carrier transport. Based on these advancements, we constructed pure Sn perovskite solar cells with a high efficiency of 5.94% and enhanced stability sustained over 100 h. The strategies used in this work to fabricate highly oriented low-dimensional films are promising for the development of high performance stable PSCs and other optoelectronic devices, especially those based on Sn perovskites. We anticipate that, with effective encapsulation, the long-term stability of Sn PSCs can be realized.

DOI: 10.1021/jacs.7b01815
J. Am. Chem. Soc. XXXX, XXX, XXX−XXX

EXPERIMENTAL DETAILS

Materials were obtained as follows: Triton X-100 (Sigma/VETEC, RG), deionized water (purite dispenser, >18 MΩ), ethylene glycol (Sigma-Aldrich, 99.5%), *N*,*N*-dimethylformamide (DMF) (Sigma-Aldrich, anhydrous, 99.8%), dimethyl sulfoxide (DMSO) (Sigma-Aldrich, anhydrous, 99.9%), tin fluoride (SnF_2) (Macklin, 99.9%), toluene (Sigma-Aldrich, HPLC, 99.9%), chlorobenzene (Sigma-Aldrich, anhydrous, 99.8%), PCBM (Nano-C, 99%). Other chemicals were purchased from Sinopharm chemical reagent Co. Ltd.

Tin Iodide (SnI_2). SnI_2 was prepared according to literature.[47]

Formamidinium Iodide ($CH(NH_2)_2I$, FAI). First, 9.3 mL of hydriodic acid was added into a 50 mL round-bottom flask which contained 5.2 mg of formamidine acetate and then was stirred for 20 min at room temperature. The white precipitate was recovered by evaporating the reaction mixture at 90 °C for 10 min. The product was dissolved in ethanol and recrystallized by ethyl acetate. After recrystallized twice, the resulting FAI was collected by filtration and dried at 60 °C overnight in a vacuum oven.

Phenylethylammonium Iodide (PEAI). PEAI was synthesized according to literature.[35] PEAI was prepared by modifying this detailed procedure for the synthesis of FAI by replacing formamidine acetate with phenethylamine and dissolving in ethanol before adding hydriodic acid. The reaction was proceeded at 0 °C. Diethyl ether was chosen for recrystallization.

NiO_x Film Fabrication. NiO_x precursor solution was prepared according to literature.[48] Nickel(II) nitrate hexahydrate ($Ni(NO_3)_2 \cdot 6H_2O$) and ethylenediamine were dissolved in ethylene glycol solution in 1:1 molar ratio and stirred at 70 °C for 3 h in oil bath to attain a 1 M precursor solution. The solution was spin-coated onto an ITO substrate at 2,000 rpm for 90 s and then baked at 300 °C for 1 h in a muffle furnace. All the NiO_x substrates were treated in an UVO machine for 9 min and transferred into the glovebox immediately for perovskite film fabrication.

Perovskite Film Fabrication. SnI_2, FAI, PEAI, and SnF_2 were dissolved in mixed solvent (DMF: DMSO = 4:1) in the molar ratio of $1:(1-x):x:0.1$ ($0 \le x \le 1$) and stirred at 70 °C for 1 h to yield a 0.6 M precursor solution. For the film fabrication, the resulting solution was filtered with a 0.22 μm PTFE filter and coated onto the substrate via a one-step spin coating process, 1000 and 5000 rpm for 10 and 30 s, respectively. During the second process, 800 μL of toluene was dropped in the middle of the substrate. The substrate was annealed at 100 °C for 30 min. All the processes were performed in a glovebox ($O_2 \le 1$ ppm, $H_2O \le 0.1$ ppm).

Device Fabrication. Indium tin oxide (ITO)-coated glasses were held in a slides holder and cleaned by ultrasonication in a deionized water bath with 4% Triton X-100 by volume, followed by an isopropanol bath and finally a deionized water bath. Each step takes 30 min. The cleaned ITO glasses were treated by oxygen plasma for 5 min before depositing the NiO_x layer. All the prepared NiO_x films were transferred into the glovebox immediately for the following fabrication processes. After the fabrication of perovskite layer, PCBM was spin-cast at 2000 rpm for 60 s from a 10 mg/mL chlorobenzene solution, followed by annealing at 80 °C for 5 min. Finally, Al (100 nm) was deposited through a mask via thermal evaporation at a rate of 0.2–0.8 Å/s to produce 0.05 cm^2 pixels. The large area (0.13 cm^2) device is also fabricated, showing the PCE deviation of less than 0.5%. Device Characterization can be found in Supporting Information.

GIWAXS. Giwaxs studies were performed at Shanghai Synchrotron Radiation Facility, Shanghai, China, using a beam energy of 10 keV (λ = 1.2398 Å). Images were acquired with a 30 s (for 0%, 20%, 40%, and 60% samples) or 10 s (for 80% and 100% samples) exposure time using a Mar 225 detector. A coin was used to shade the center area of the diffraction patterns. The distance between the sample and detector was 360 mm. The grazing incidence angles for 0%, 20%, 40%, 60%, 80%, and 100% films were 0.2°, 0.3°, 0.3°, 0.3°, 1.0°, and 0.2°, respectively. Other characterizations can be found in Supporting Information.

First-Principles Calculations. First-principles calculations are performed within the framework of density functional theory (DFT) using plane-wave pseudopotential methods as implemented in the Vienna Ab-initio Simulation Package.[49,50] The electron–ion interaction is described by the projected augmented pseudopotential method,[51] and electron configurations of $5s^25p^2$ for Sn, $5s^25p^5$ for I, $2s^22p^2$ for C, $2s^22p^3$ for N, and 1s for H are considered as valence electrons. The generalized gradient approximation formulated by Perdew, Burke, and Ernzerhof[52] is used as the exchange-correlation functional. The electronic wave functions are expended in plane-wave basis sets with kinetic energy cutoff of 400 eV. The Monkhorst–Pack k-point meshes with grid spacing of $2\pi \times 0.04$ $Å^{-1}$ or less are used for electronic Brillouin zone integration. The equilibrium structural parameters (including both lattice parameters and internal coordinates) of each involved material are obtained via total energy minimization by using the conjugate-gradient algorithm, with the force convergence threshold of 0.01 eV/Å. To properly take into account the long-range van der Waals interaction that plays a non-ignorable role in the hybrid perovskites involving organic molecules, the vdWs-optB86b functional[53] is adopted.

ASSOCIATED CONTENT

Supporting Information

The Supporting Information is available free of charge on the ACS Publications website at DOI: 10.1021/jacs.7b01815.

Experimental details and additional supplementary figures (PDF)

AUTHOR INFORMATION

Corresponding Authors

*lijun_zhang@jlu.edu.cn

*ningzhj@shanghaitech.edu.cn

ORCID

Zhifang Shi: 0000-0003-1673-0983

Lijun Zhang: 0000-0002-6438-5486

Zhijun Ning: 0000-0002-9130-3490

Author Contributions

⊥These authors contributed equally.

Notes

The authors declare no competing financial interest.

ACKNOWLEDGMENTS

The authors gratefully acknowledge financial support from the National Key Research and Development Program of China (under Grants No. 2016YFA0204000 and 2016YFB0201204), ShanghaiTech start-up funding, 1000 young talent program, National Natural Science Foundation of China (U1632118, 21571129), Shanghai key research program (16JC1402100), Shanghai International Cooperation Project (16520720700), and National Natural Science Foundation of China (under Grants No. 11404131 and 11674121). The authors appreciate Shanghai Synchrotron Radiation Facility, China. The authors appreciate the Test Center of ShanghaiTech University and Dr. Peihong Cheng. Calculations were performed in the high-performance computing center of Jilin University.

REFERENCES

(1) Dong, Q.; Fang, Y.; Shao, Y.; Mulligan, P.; Qiu, J.; Cao, L.; Huang, J. *Science* **2015**, *347*, 967–970.

(2) Yin, W.-J.; Shi, T.; Yan, Y. *Appl. Phys. Lett.* **2014**, *104*, 063903.

(3) Wehrenfennig, C.; Eperon, G. E.; Johnston, M. B.; Snaith, H. J.; Herz, L. M. *Adv. Mater.* **2014**, *26*, 1584–1589.

(4) Takahashi, Y.; Hasegawa, H.; Takahashi, Y.; Inabe, T. *J. Solid State Chem.* **2013**, *205*, 39–43.

(5) Lim, K. G.; Kim, H. B.; Jeong, J.; Kim, H.; Kim, J. Y.; Lee, T. W. *Adv. Mater.* **2014**, *26*, 6461–6466.

DOI: 10.1021/jacs.7b01815
J. Am. Chem. Soc. XXXX, XXX, XXX–XXX

(6) Lim, K. G.; Ahn, S.; Kim, Y. H.; Qi, Y.; Lee, T. W. *Energy Environ. Sci.* **2016**, *9*, 932−939.
(7) Kim, H.; Lim, K. G.; Lee, T. W. *Energy Environ. Sci.* **2016**, *9*, 12−30.
(8) Lim, K. G.; Ahn, S.; Kim, H.; Choi, M. R.; Huh, D. H.; Lee, T. W. *Adv. Mater. Interfaces* **2016**, *3*, 1500678.
(9) Green, M. A.; Ho-Baillie, A.; Snaith, H. J. *Nat. Photonics* **2014**, *8*, 506−514.
(10) Snaith, H. J. *J. Phys. Chem. Lett.* **2013**, *4*, 3623−3630.
(11) Liu, M.; Johnston, M. B.; Snaith, H. J. *Nature* **2013**, *501*, 395−398.
(12) Kojima, A.; Teshima, K.; Shirai, Y.; Miyasaka, T. *J. Am. Chem. Soc.* **2009**, *131*, 6050−6051.
(13) Gao, P.; Grätzel, M.; Nazeeruddin, M. K. *Energy Environ. Sci.* **2014**, *7*, 2448−2463.
(14) Liao, W.; Zhao, D.; Yu, Y.; Grice, C. R.; Wang, C.; Cimaroli, A. J.; Schulz, P.; Meng, W.; Zhu, K.; Xiong, R. G.; Yan, Y. *Adv. Mater.* **2016**, *28*, 9333−9340.
(15) Öz, S.; Hebig, J.-C.; Jung, E.; Singh, T.; Lepcha, A.; Olthof, S.; Jan, F.; Gao, Y.; German, R.; van Loosdrecht, P. H. M.; Meerholz, K.; Kirchartz, T.; Mathur, S. *Sol. Energy Mater. Sol. Cells* **2016**, *158*, 195−201.
(16) Zhu, H. X.; Liu, J. M. *Sci. Rep.* **2016**, *6*, 37425.
(17) Cortecchia, D.; Dewi, H. A.; Yin, J.; Bruno, A.; Chen, S.; Baikie, T.; Boix, P. P.; Gratzel, M.; Mhaisalkar, S.; Soci, C.; Mathews, N. *Inorg. Chem.* **2016**, *55*, 1044−1052.
(18) Hao, F.; Stoumpos, C. C.; Cao, D. H.; Chang, R. P. H.; Kanatzidis, M. G. *Nat. Photonics* **2014**, *8*, 489−494.
(19) Noel, N. K.; Stranks, S. D.; Abate, A.; Wehrenfennig, C.; Guarnera, S.; Haghighirad, A.-A.; Sadhanala, A.; Eperon, G. E.; Pathak, S. K.; Johnston, M. B.; et al. *Energy Environ. Sci.* **2014**, *7*, 3061−3068.
(20) Kumar, M. H.; Dharani, S.; Leong, W. L.; Boix, P. P.; Prabhakar, R. R.; Baikie, T.; Shi, C.; Ding, H.; Ramesh, R.; Asta, M.; Graetzel, M.; Mhaisalkar, S. G.; Mathews, N. *Adv. Mater.* **2014**, *26*, 7122−7127.
(21) Koh, T. M.; Krishnamoorthy, T.; Yantara, N.; Shi, C.; Leong, W. L.; Boix, P. P.; Grimsdale, A. C.; Mhaisalkar, S. G.; Mathews, N. *J. Mater. Chem. A* **2015**, *3*, 14996−15000.
(22) Lee, S. J.; Shin, S. S.; Kim, Y. C.; Kim, D.; Ahn, T. K.; Noh, J. H.; Seo, J.; Seok, S. I. *J. Am. Chem. Soc.* **2016**, *138*, 3974−3977.
(23) Ergen, O.; Gilbert, S. M.; Pham, T.; Turner, S. J.; Tan, M. T. Z; Worsley, M. A.; Zettl, A. *Nat. Mater.* **2016**, *16*, 522.
(24) Hao, F.; Stoumpos, C. C.; Guo, P.; Zhou, N.; Marks, T. J.; Chang, R. P. H.; Kanatzidis, M. G. *J. Am. Chem. Soc.* **2015**, *137*, 11445−11452.
(25) Yang, J.; Siempelkamp, B. D.; Liu, D.; Kelly, T. L. *ACS Nano* **2015**, *9*, 1955−1963.
(26) Christians, J. A.; Miranda Herrera, P. A.; Kamat, P. V. *J. Am. Chem. Soc.* **2015**, *137*, 1530−1538.
(27) Leguy, A. M. A.; Hu, Y.; Campoy-Quiles, M.; Alonso, M. I.; Weber, O. J.; Azarhoosh, P.; Van Schilfgaarde, M.; Weller, M. T.; Bein, T.; Nelson, J.; Docampo, P.; Barnes, P. R. F. *Chem. Mater.* **2015**, *27*, 3397−3407.
(28) Zhao, L.; Kerner, R. A.; Xiao, Z.; Lin, Y. L.; Lee, K. M.; Schwartz, J.; Rand, B. P. *ACS Energy Lett.* **2016**, *1*, 595−602.
(29) Liu, Z.; Sun, B.; Shi, T.; Tang, Z.; Liao, G. *J. Mater. Chem. A* **2016**, *4*, 10700−10709.
(30) Mitzi, D. B.; Feild, C.; Harrison, W.; Guloy, A. *Nature* **1994**, *369*, 467−469.
(31) Kagan, C. R.; Mitzi, D. B.; Dimitrakopoulos, C. D. *Science* **1999**, *286*, 945−947.
(32) Mitzi, D. B. *J. Solid State Chem.* **1999**, *145*, 694−704.
(33) Smith, I. C.; Hoke, E. T.; Solis-Ibarra, D.; McGehee, M. D.; Karunadasa, H. I. *Angew. Chem.* **2014**, *126*, 11414−11417.
(34) Cao, D. H.; Stoumpos, C. C.; Farha, O. K.; Hupp, J. T.; Kanatzidis, M. G. *J. Am. Chem. Soc.* **2015**, *137*, 7843−7850.
(35) Quan, L. N.; Yuan, M.; Comin, R.; Voznyy, O.; Beauregard, E. M.; Hoogland, S.; Buin, A.; Kirmani, A. R.; Zhao, K.; Amassian, A.; Kim, D. H.; Sargent, E. H. *J. Am. Chem. Soc.* **2016**, *138*, 2649−2655.
(36) Milot, R. L.; Sutton, R. J.; Eperon, G. E.; Haghighirad, A. A.; Martinez Hardigree, J.; Miranda, L.; Snaith, H. J.; Johnston, M. B.; Herz, L. M. *Nano Lett.* **2016**, *16*, 7001−7007.
(37) Tsai, H.; Nie, W.; Blancon, J.-C.; Stoumpos, C. C.; Asadpour, R.; Harutyunyan, B.; Neukirch, A. J.; Verduzco, R.; Crochet, J. J.; Tretiak, S.; et al. *Nature* **2016**, *536*, 312−316.
(38) Wooten, F. *Optical Properties of Solids*; Academic Press: New York, 2013.
(39) Zhang, J.; Xiong, Z.; Zhao, X. S. *J. Mater. Chem.* **2011**, *21*, 3634−3640.
(40) Kobayashi, Y.; Salgueiriño-Maceira, V.; Liz-Marzán, L. M. *Chem. Mater.* **2001**, *13*, 1630−1633.
(41) Šeruga, M.; Metikoš-Huković, M.; Valla, T.; Milun, M.; Hoffschultz, H.; Wandelt, K. J. *Electroanal. Chem.* **1996**, *407*, 83−89.
(42) Marshall, K. P.; Walker, M.; Walton, R. I.; Hatton, R. A. *Nat. Energy* **2016**, *1*, 16178.
(43) Zhou, H.; Chen, Q.; Li, G.; Luo, S.; Song, T.-b.; Duan, H.-S.; Hong, Z.; You, J.; Liu, Y.; Yang, Y. *Science* **2014**, *345*, 542−546.
(44) Bi, D.; Tress, W.; Dar, M. I.; Gao, P.; Luo, J.; Renevier, C.; Schenk, K.; Abate, A.; Giordano, F.; Baena, J.-P. C.; Decoppet, J.-D.; Gratzel, M.; Hagfeldt, A.; et al. *Sci. Adv.* **2016**, *2*, e1501170.
(45) Chen, W.; Wu, Y.; Yue, Y.; Liu, J.; Zhang, W.; Yang, X.; Chen, H.; Bi, E.; Ashraful, I.; Grätzel, M.; Han, L. *Science* **2015**, *350*, 944−948.
(46) Zhang, M.; Lyu, M.; Yun, J.-H.; Noori, M.; Zhou, X.; Cooling, N. A.; Wang, Q.; Yu, H.; Dastoor, P. C.; Wang, L. *Nano Res.* **2016**, *9*, 1570−1577.
(47) Stoumpos, C. C.; Malliakas, C. D.; Kanatzidis, M. G. *Inorg. Chem.* **2013**, *52*, 9019−9038.
(48) You, J.; Meng, L.; Song, T.-B.; Guo, T.-F.; Yang, Y. M.; Chang, W.-H.; Hong, Z.; Chen, H.; Zhou, H.; Chen, Q.; Liu, Y.; Marco, N. D.; Yang, Y. *Nat. Nanotechnol.* **2016**, *11*, 75−81.
(49) Kresse, G.; Furthmüller. *Phys. Rev. B: Condens. Matter Mater. Phys.* **1996**, *54*, 11169.
(50) Kresse, G.; Furthmüller. *Comput. Mater. Sci.* **1996**, *6*, 15−50.
(51) Blöchl, P. E. *Phys. Rev. B: Condens. Matter Mater. Phys.* **1994**, *50*, 17953−17979.
(52) Perdew, J. P.; Burke, K.; Ernzerhof, M. *Phys. Rev. Lett.* **1996**, *77*, 3865−3868.
(53) Klimes, J.; Bowler, D. R.; Michaelides, A. *J. Phys.: Condens. Matter* **2010**, *22*, 022201.

DOI: 10.1021/jacs.7b01815
J. Am. Chem. Soc. XXXX, XXX, XXX−XXX